Three-dimensional self-accelerating acoustic beam based on artificial Archimedean-spiral slits

Di-Chao Chen,[1,2] Hao-Yue Zhu,[2] Da-Jian Wu,[2,*] Xing-Feng Zhu,[2] Ying Cheng,[1] and Xiao-Jun Liu[1,†]

[1] *Institute of Acoustics, Department of Physics, Nanjing University, Nanjing 210093, China*

[2] *Jiangsu Key Lab of Opto-Electronic Technology, School of Physics and Technology, Nanjing Normal University, Nanjing 210023, China*

(Received 31 October 2023; revised 29 December 2023; accepted 21 February 2024; published 14 March 2024)

Self-accelerating acoustic beams (SABs) are capable of transporting particles directionally and transmitting acoustic signals and energy along curved paths. However, the majority of prior SABs have only been able to deflect within a two-dimensional plane, with lateral acceleration impacted by the operating frequency and transverse plane size of the sound source. Here, we are committed to using designed acoustic artificial structure plates to achieve self-accelerating beams with three-dimensional (3D) helical trajectories, also known as acoustic radial self-accelerating beams. To manipulate the shape of the main lobe of a 3D self-accelerating beam, we introduce the notion of asymmetric Bessel into radial self-accelerating beams, resulting in the successful derivation of analytical expressions for acoustic radial self-accelerating asymmetric Bessel beams (RS-ABBs) propagating in free space. An artificial plate structure, engraved with Archimedean-spiral slits, is designed to produce acoustic RS-ABBs in reality. Finally, the numerical and experimental measurements of acoustic intensity field distributions for the generated acoustic RS-ABBs are demonstrated. The study outlined here can greatly benefit the development of techniques in acoustic particle manipulation, and can also offer inspiration for distance measurement, acoustic sensing, and acoustic communication.

DOI: 10.1103/PhysRevApplied.21.034025

I. INTRODUCTION

Self-accelerating acoustic beams (SABs) with curved propagation trajectories have attracted growing interest in the past decade [1–6]. With the acoustic radiation force exerted by the SAB, particle trapping [1,2] and directional transportation of microbubbles [3] can be experimentally realized [7,8]. SABs are capable of transmitting acoustic signals along curved paths and circumventing obstacles [4]. In addition, the curved path and nondiffraction of SABs during propagation are especially beneficial for the collection of sound energy [5] and have been explored for medical ultrasound [6]. The vast majority of SABs currently consider the characteristics of lateral acceleration during field propagation, that is, the SABs deflect in a two-dimensional plane, including the well-known Airy beams [9–11], Weber beams [12], Mathieu beams [13], Bessel beams [14], vector beams [15], and beams with arbitrary transverse shapes [16–19]. Nevertheless, by definition, lateral acceleration is always coupled to the lateral range of the acoustic field. That is, the greater the acceleration, the larger the propagation angle, and then the transverse plane of space is unbounded.

For limitations that require the use of unbounded transverse planes, an efficient approach is to confine the motion of the SAB to the azimuthal degrees of freedom by creating rotational fields. This approach, which converts a two-dimensional SAB into a three-dimensional one, provides fresh viewpoints and possibilities for manipulating acoustic wave fronts and may open an avenue to the development of SABs. In recent years, optical radial self-accelerating beams (RSABs) based on this angular velocity rotating field theory have been widely developed and promoted [20–24]. The realized optical RSABs propagate along spiraling trajectories due to radial acceleration [21,22], and the beams can further acquire angular acceleration while rotating around the axis [23,24]. The advantage of these classes of beams is that the acceleration is not directly coupled to the size of the field and can be tuned to very high values; consequently, the velocity of rotation around the optical axis of the RSABs and the angular acceleration can be arbitrarily modulated. This unique set of properties has proven useful in various fields of application and research, such as sensing [25], optical trapping and tweezing [26], and imaging [27]. To achieve RSABs, it is necessary to superimpose beams with different axial

*wudajian@njnu.edu.cn
†liuxiaojun@nju.edu.cn

wave numbers. Typically, digital holography and spatial light modulators can regulate the amplitude and phase of transmitted light waves, thus realizing control of the axial wave number of light waves. In contrast to an easily controlled optical wave front, the simultaneous modulation of acoustic amplitude and phase is considered challenging. Although acoustic micrometamaterial units proposed in recent years can realize simultaneous control of amplitude and phase, the structural size of the smallest unit and the complexity of the structure restrict their further applications [16,17]. Additionally, different shapes of RASBs are essential in practical applications, including particle manipulation and acoustic energy transmission. The modulation of RASB shapes is currently an urgent issue that requires attention.

In this work, we present the idea of employing the concept of asymmetric Bessel [28–31] in RSABs, successfully creating radial self-accelerating asymmetric Bessel beams (RS-ABBs). The shape of the main lobe of RS-ABBs can be modified independently by adjusting the asymmetry parameters [31]. Additionally, we develop artificial structure plates with Archimedean-spiral slits to produce acoustic RS-ABBs, as illustrated in Fig. 1. The requirements of orders and axial wave number of superimposed Bessel modes of RS-ABBs can be fulfilled by adjusting the number of arms and initial radius of the combined Archimedean-spiral slits. Experimental and numerical demonstrations confirm the ability of the artificial structure plates to generate RS-ABBs.

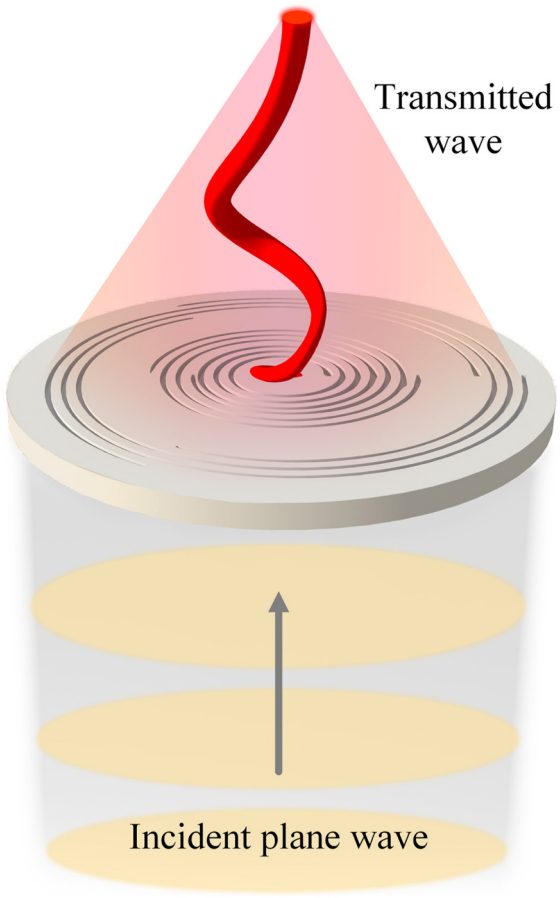

FIG. 1. Schematic diagram of the propagation of the RS-ABB generated by an artificial structure.

II. GENERAL FORMULA OF SELF-ACCELERATING ASYMMETRIC BESSEL BEAMS

First, we conduct an extensive theoretical derivation of the most general expression for acoustic RS-ABBs. A complex acoustic field is modeled, which is invariant in a rotationally moving frame. The wave propagating in this acoustic field is supposed to be the solution of the scalar Helmholtz equation $(\nabla^2 + k^2)P = 0$, where P is the acoustic field and $k = 2\pi/\lambda$ is the wave number of the acoustic wave with wavelength λ. Considering the cylindrical coordinate system, a solution of the scalar Helmholtz equation in the form of a Bessel mode can be written as [28,31]

$$P_n(r,\theta,z) = \exp(in\theta + ik_z z)J_n(k_r r), \tag{1}$$

where k_z and k_r are the axial and radial wave numbers $({k_z}^2 + {k_r}^2 = k^2)$, respectively, and J_n is the nth-order Bessel function of the first kind. According to the superposition principle, any linear superposition of Bessel modes in Eq. (1) is also a solution of the scalar Helmholtz equation. Therefore, we can write the most general solution of the scalar Helmholtz equation as

$$P(r,\theta,z) = \sum_{n=0}^{\infty} C_0 \exp(in\theta + ik_z z)J_n(k_r r). \tag{2}$$

Here, $J_n(k_r r)\exp(in\theta + ik_z z)$ are the cylindrical eigenmodes [20], whose propagation constants are given by k_z. Moreover, for an arbitrary beam, the expansion coefficients C_0 are arbitrary.

For RS-ABBs, we can discuss two aspects of radial self-accelerating and asymmetric Bessel. The realization of the radial self-accelerating beam needs to satisfy three main generation conditions, namely no external potential or nonlinear acoustic effects, nondiffraction of the beams, and the existence of fictitious forces. Since the scalar Helmholtz equation is linear and time independent, the solution of it satisfies the requirement of nonlinear acoustic effects. For the second condition, to make P independent of the propagation direction, we need to perform a coordinate transformation, by which the acoustic field distribution is no longer dependent on the propagation distance thus satisfying the no-diffraction condition and theoretically realizing a self-accelerating helical acoustic beam. An acoustic field of the form $P(r,\theta,z) = P(r,\theta+\omega z) = P(r,\theta')$ fulfills this

condition. Furthermore, since the above coordinate transformation describes a frame of reference that rotates at an angular velocity ω, the effect of centrifugal force can be generated, and the last condition is satisfied.

Comparing the coordinate-transformed equation $P(r,\theta,z) = P(r,\theta+\omega z)$ with Eq. (2), we obtain $k_z = n\omega$. When k_z is constrained to be positive, the signs of n and ω are equal. Since k_z is a function of k_r, k_r can be rewritten as $k_r = \sqrt{k^2 - \omega^2 n^2}$. To make the acoustic intensity rotate during the propagation process, the selection of the axial wave number should fulfill specific requirements, and the angular velocity along the propagation axis can be given by $\omega = \Delta k_z/\Delta n$ [20,32]. It is observed that the magnitude of the angular velocity is related to the difference between the adjacent Bessel orders Δn. Applying the restrictions on angular velocity along the propagation direction, Eq. (2) becomes

$$P(r,\theta+\omega z) = \sum_{m=0}^{\infty} C_0 J_{l+m}(k_r r)\exp[il(\theta+\omega z) + im(\theta+\omega z)], \quad (3)$$

where $n = l+m$, l is the initial Bessel order, and m is the increased order to the initial Bessel order. This is the general expression for a radial self-accelerating beam propagating in space with a rotational angular velocity ω.

Next, we further discuss the realization of asymmetric Bessel beams on this basis. Since the expansion coefficient C_0 of the superimposed Bessel modes can be arbitrary, we set the expansion coefficient C_0 in Eq. (3) to be $c^m/m!$, and Eq. (3) can be rewritten as

$$P(r,\theta+\omega z) = \sum_{m=0}^{\infty} \frac{c^m}{m!}\exp[il(\theta+\omega z) + im(\theta+\omega z)]J_{l+m}(k_r r), \quad (4)$$

where c is the scaling factor, which is assumed to be a positive real constant and determines the degree of asymmetry of the Bessel beam. We can rewrite Eq. (4) by using the reference integral formula

$$\sum_{m=0}^{\infty} \frac{t^m}{m!} J_{n+m}(x) = x^{n/2}(x-2t)^{-n/2} J_n\left(\sqrt{x^2-2tx}\right). \quad (5)$$

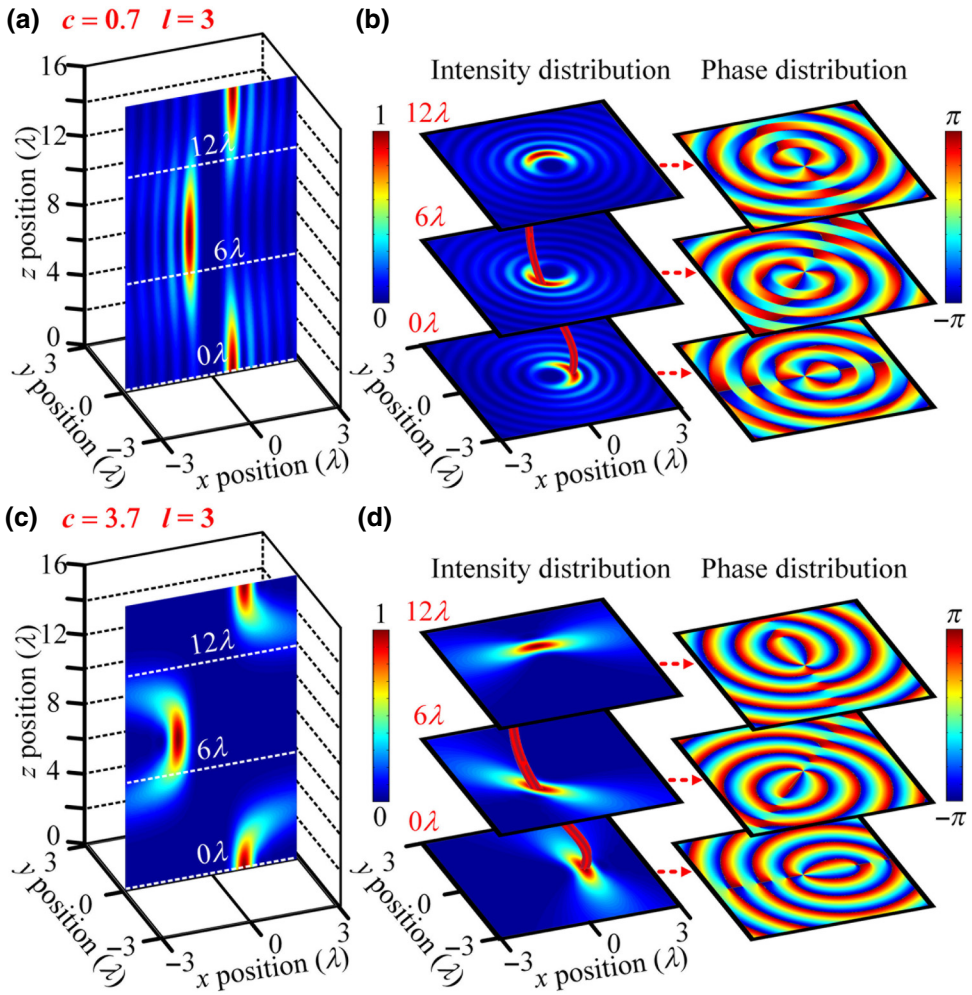

FIG. 2. Analytical acoustic intensity distributions of the RS-ABB with $c = 0.7$ (a) in the x-z plane and (b) at three transverse planes of $z = 0$, $z = 6\lambda$, and $z = 12\lambda$. Analytical acoustic intensity distributions of the RS-ABB with $c = 3.7$ (c) in the x-z plane and (d) at three transverse planes of $z = 0$, $z = 6\lambda$, and $z = 12\lambda$.

Equation (4) is reduced to

$$P(r,\theta+\omega z;c)=\left[\frac{k_r r}{k_r r-2c\exp[i(\theta+\omega z)]}\right]^{l/2}\times J_l\left\{\sqrt{k_r r[k_r r-2c\exp[i(\theta+\omega z)]]}\right\}\times\exp[il(\theta+\omega z)]. \quad (6)$$

This is the most general analytic expression of the RS-ABB that rotates in free space with an angular velocity ω. Apparently, when $\omega=0$, Eq. (6) can be simplified to the expression of a general asymmetric Bessel beam with a crescent-shaped intensity distribution, but not rotating with the propagation distance [28–31]. From Eq. (6), the order of the RS-ABB is the same as the initial Bessel order. In addition, the axial wave number $l\omega$ of the initial Bessel order does not affect the acoustic intensity distribution of the RS-ABB. Therefore, when only the rotational intensity acoustic field is considered, the axial wave number of the nth-order Bessel beam can be further rewritten as $k_z=m\omega+l\omega_0$. Here, ω_0 represents the angular velocity of the initial Bessel order, which may differ from ω. The dimensionless quantity c is the asymmetry parameter, which can modify the amplitude distribution and the azimuthal distribution. The acoustic intensity profile of the RS-ABB with $c=0.7$ in the x-z plane based on Eq. (6) is shown in Fig. 2(a). Figure 2(b) shows the acoustic phase and intensity distributions of RS-ABBs at the corresponding three different planes. The intensity of the RS-ABB features a crescent shape. Figures 2(c) and 2(d) show the acoustic phase and intensity distributions of RS-ABBs with $c=3.7$. The initial Bessel orders of $c=0.7$ and $c=3.7$ are both $l=3$. When c increases, the RS-ABB becomes more asymmetric and the off-axis distance increases, which is consistent with the asymmetric Bessel beams reported in Ref. [31]. However, the difference is that the RS-ABB has an angular velocity ω. The crescent-shaped RS-ABB gradually rotates as the transmission distance increases. In this work, we set the counterclockwise direction as the positive direction of rotation. Figures 2(b) and 2(d) show the phase and intensity distributions at $z=0$, 6λ, and 12λ, where the angular velocities ω are fixed as $-\pi/8\lambda$. To distinguish ω_0 from ω, we fix ω_0 as $-\pi/16\lambda$. Of course, the angular velocities ω can also be variables in the forms of functions, which will give the RS-ABB an angular acceleration. During the propagation of RS-ABBs, the deformation of the phase at different positions originates from the initial angular velocity ω_0, and the acoustic intensity is not affected by ω_0 [20]. In addition, we investigate the effect of operating frequency on the RS-ABB and find that the size of the crescent-shaped RS-ABB decreases with increasing operating frequency (not shown). Based on the above discussion results, Eq. (6) can describe RS-ABBs of free space, where the asymmetry parameter c governs the asymmetry degree of the mode and the angular velocity ω determines the rotational speed of the crescent-shaped acoustic intensity.

III. SIMPLIFICATION OF THE SUPERIMPOSED BESSEL MODES

It can be seen from Eq. (4) that the RS-ABBs consist of infinite Bessel modes of different orders, and each Bessel mode has a specific amplitude. In the process of practical realization, the simultaneous superimposition of these Bessel modes is challenging. Here, for this problem, we propose a feasible strategy to realize RS-ABBs by superimposing Bessel modes with particular orders and uniform transmission amplitudes. This approach will be more practical in different scenarios and provide more freedom of control. Figure 3(a) shows the general scheme for implementing RS-ABBs using a simplified method. It is known from Eq. (4) that the amplitudes of the superimposed Bessel modes are determined by $c^m/m!$. In step 1, we show a two-dimensional plot of the amplitude distribution of the Bessel modes as a function of asymmetry parameter c and increased order m. With increasing c, the maximum amplitude of the superimposed Bessel modes increases. To better observe the amplitude distribution of each constituent Bessel mode under different c values, in step 2, we normalize the amplitude of the constituent Bessel modes with the amplitude maxima at the respective c value. It is seen that with increasing c value, the m value corresponding to the maximum amplitude increases, and the full width at half maximum (FWHM) increases gradually. From step 2, we find that for different c values, only a few Bessel modes dominate, and most Bessel modes are negligible due to their small amplitudes. Therefore, we plan to adopt a simplified scheme, which is to binarize the amplitudes of the superimposed Bessel modes. We should note that when c is small (i.e., when there are fewer dominant Bessel modes), performing a two-bit approximation is sufficient to well produce the RS-ABB, and that as the number of approximation bits increases, the RS-ABB obtained will converge more and more to the untruncated accurate result (see Appendix A). In step 3, we take half of the maximum amplitude of the constituent Bessel mode at different c values as the reference value, and binarize the amplitudes of Bessel modes of different orders. The Bessel modes with amplitudes less than or equal to the reference value are ignored, while Bessel modes with amplitudes greater than the reference value are retained and the amplitude is set to 1. The Bessel modes that need to be superimposed can be determined through the processed amplitudes. In this way we transform an infinite number of Bessel modes with specific amplitudes into a finite number of Bessel modes with uniform amplitudes.

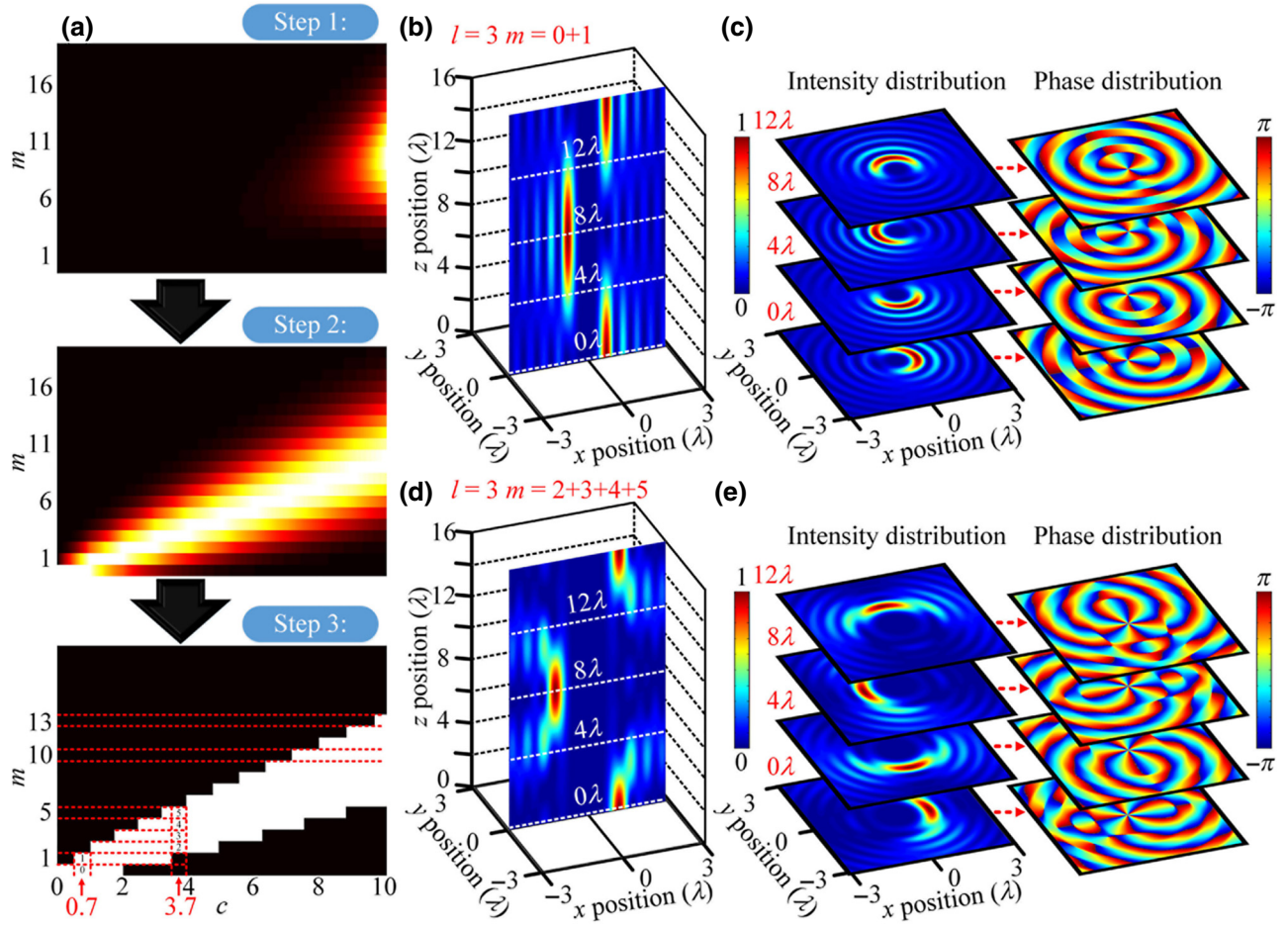

FIG. 3. (a) The general scheme of the simplified method for implementing the RS-ABB. Acoustic intensity and phase distributions of the RS-ABB with (b),(c) $c = 0.7$ and (d),(e) $c = 3.7$ obtained by the simplified method.

Then, we further verify the feasibility of the scheme. Referring to step 3, we obtain that when the asymmetry parameters c are 0.7 and 3.7, the composition of the increased orders m are (0, 1) and (2, 3, 4, 5), respectively. In addition, the initial Bessel order l is fixed to 3 (in keeping with Fig. 2), so the final compositions of the Bessel modes are (3, 4) and (5, 6, 7, 8), respectively. Figures 3(b)–3(e) are the RS-ABBs of $c = 0.7$ and 3.7 obtained by the simplified scheme, which specifically show the acoustic phase and intensity distributions of the RS-ABBs at four transverse planes of $z = 0$, $z = 4\lambda$, $z = 8\lambda$, and $z = 12\lambda$. Compared with the results in Fig. 2, the generated RS-ABBs are basically the same. Three characteristics of RS-ABBs are observed, namely the acoustic intensity distribution is crescent-shaped, the asymmetry and the off-axis distance increase with the c value, and the crescent-shaped intensity rotates around the axis during transmission. We also observe that as the value of c increases, the difference between the phase and intensity distribution in Figs. 3 and 2 also increases. The main reason is that the FWHM gradually increases as c increases. This leads to an increase in the number of superimposed Bessel modes and hence the error caused due to the different k_r of these modes increases gradually. Additionally, the amplitude variation flattens, causing an increase in error when obtaining the amplitude based on binarization. In addition, it is worth noting that due to the binarization of the amplitude, the superposition of different Bessel modes corresponds to a range of c values rather than a single value, as shown in step 3. Second, the initial Bessel order l affects the choice of asymmetry parameter c; for example, the final compositions of the Bessel modes (5, 6, 7, 8) can also be obtained by adding the initial order 4 and increased orders (1, 2, 3, 4). Therefore, when the final composition of the Bessel modes is known, we have to determine the initial order l before considering the asymmetry parameter c. Here, we fix the angular velocity $[\omega = (k_z - l\omega_0)/m]$ to $-\pi/8\lambda$. As ω increases, n and $l\omega_0$ remain constant and k_z increases, and when the value of k_z exceeds the wave number k, it will not be possible to generate RS-ABBs. Therefore, for the effective realization of the RS-ABB, the value of $(\omega m + l\omega_0)$ should be less than k

when setting the parameters. In general, the above results demonstrate that RS-ABBs can also be well implemented by using a finite number of Bessel modes with uniform amplitudes.

IV. DESIGN THEORY OF ARTIFICIAL STRUCTURE PLATE

The second requirement to implement RS-ABBs is that each superimposed Bessel mode has a specific axial wave number k_z. Previous studies have shown that acoustic artificial structures with Archimedes spirals can realize the conversion between acoustic plane beams and acoustic Bessel vortex beams [33–35]. However, most previous studies have focused on the surface field distribution of acoustic artificial structural plates, without considering the changes in k_r and k_z during propagation and the effect of k_r and k_z changes on the generated Bessel vortex beams. The variation in k_r and k_z with the propagation distance and the influencing factors are the focus of the research in this section, and a detailed theoretical analysis is given below. Figure 4(a) shows the schematics of the artificial structures for achieving Bessel vortex beams with different topological charge values (n). It can be seen that the topological charge n of the Bessel vortex beams corresponds to the number of arms of the Archimedes-spiral slits. The orbit of the innermost Archimedes-spiral slit can be expressed in polar coordinates as [35]

$$r(\phi) = r_0 + \frac{na}{2\pi}\left(\phi - \frac{2\pi}{n}i\right), \quad \left(\frac{i}{n}2\pi \le \phi \le \frac{i+1}{n}2\pi\right), \tag{7}$$

where r and ϕ are the radial and azimuthal coordinates of the spiral slits, r_0 is the initial radius, i ($0 \le i \le n-1$) is the index of the nth arm, the width of the slit is d, and a is the radial separation between arms. To facilely analyze the influence of the spiral slit on the transmitted Bessel beam, we consider the transmission case of a single-turn narrow slit, and the number of arms (n) is fixed as 1, as shown in Fig. 4(b), where α is the angle between the line connecting the transmission point and the observation point and the horizontal plane. The total transmitted field can be obtained by the coherent superposition of multiple turns. The acoustic pressure field at an observation point (L, θ, z) near the origin caused by the slit is given by [33]

$$dP = A_0 \exp(ik_z z)\frac{\exp[i\vec{k_r}\cdot(L\vec{e_L} - r\vec{e_r})]}{|L\vec{e_L} - r\vec{e_r}|}rd\phi, \tag{8}$$

where A_0 represents the amplitude of the transmission field. In the initial transmission surface of the Archimedean-spiral slit ($z = 0$), k_r is dominant, and the component of k_z is almost 0 (that is, $k = k_r = 2\pi/\lambda$).

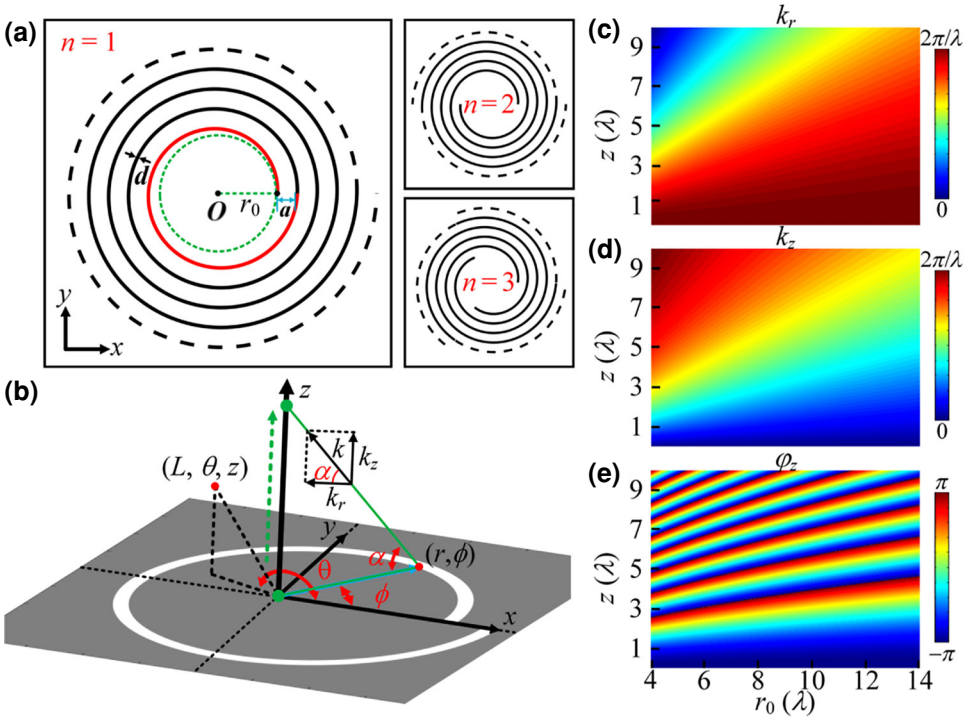

FIG. 4. (a) Schematics of the artificial structures for achieving Bessel vortex beams with $n = 1$, 2, and 3. (b) Diagram of a single-turn Archimedean spiral with $n = 1$ and the coordinates used in analytical derivation. Two-dimensional plots of (c) k_r, (d) k_z, and (e) φ_z as a function of r_0 and z.

Nevertheless, as the observation point moves along the z axis direction, k_r changes and can be expressed as $2\pi\cos(\alpha)/\lambda$. Figure 4(c) exhibits a two-dimensional plot of k_r as a function of the initial radius (r_0) and the propagation distance (z). It can be seen that both r_0 and z cause changes in k_r. With the increase in z, k_r gradually decreases, and the increase in r_0 changes the speed of decrease. Since k_z is a function of k_r, as the propagation distance z increases, k_z can be expressed as $k_z = \sqrt{k^2 - k_r^2} = (2\pi/\lambda)\sqrt{1-\cos(\alpha)^2} = (2\pi/\lambda)\sin(\alpha)$, as shown in Fig. 4(d). We denote the distance from the acoustic wave emission point to the observation point as D, which is related to the radial distance in the plane and the propagation distance z. For an observation point along the propagation axis, D can be simplified by $D = [(r_0 + a\phi/2\pi)^2 + z^2]^{1/2}$. The phase difference between two adjacent acoustic wave emission points to an observation point can be expressed as $d\varphi_r = (2\pi/\lambda)dD$. After the integration, the phase around the observation point can be expressed as $\varphi_r = 2\pi\left[\sqrt{(r_0+a)^2+z^2} - \sqrt{r_0^2+z^2}\right]/\lambda$. Therefore, with the increase in z, the valid expression of the one-arm Archimedes-spiral slit can be written as

$$r(\phi, z) = \sqrt{r_0^2 + z^2} + \frac{\left[\sqrt{(r_0+a)^2+z^2} - \sqrt{r_0^2+z^2}\right]}{2\pi}\phi.$$

Moreover, under the near-field condition, for observations along the propagation axis, $|L\overrightarrow{e_L} - r\overrightarrow{e_r}| = \sqrt{L^2 + r^2 - 2Lr}$ can be approximately equal to r. Applying these conditions, we can deduce the acoustic field expression of the observation point as

$$P(L,\theta,z) = A_0 \exp\left[i\frac{2\pi}{\lambda}\sin(\alpha)z\right]\exp\left[-i\sqrt{r_0^2+z^2}\frac{2\pi}{\lambda}\cos(\alpha)\right] \times \int_0^{2\pi} \exp[iLk_r\cos(\theta-\phi)]\exp\left[-i\frac{\left[\sqrt{(r_0+a)^2+z^2} - \sqrt{r_0^2+z^2}\right]\cos(\alpha)}{\lambda}\phi\right]d\phi. \quad (9)$$

Suppose the value of a is equal to wavelength λ, and r_0 is much greater than λ. Under the near-field condition, $\left(\sqrt{(r_0+a)^2+z^2} - \sqrt{r_0^2+z^2}\right)\cos(\alpha)$ is approximately equal to λ, and the product of $\sqrt{r_0^2+z^2}$ and $\cos(\alpha)$ is r_0; therefore Eq. (9) can be further simplified as

$$P(L,\theta,z) = A_0 \exp\left[i\frac{2\pi}{\lambda}\sin(\alpha)z\right]\exp\left[-ir_0\frac{2\pi}{\lambda}\right] \times \int_0^{2\pi} \exp[iLk_r\cos(\theta-\phi)]\exp[-i\phi]d\phi. \quad (10)$$

By using the Jacobi-Anger expansion $J_n(\gamma) = (1/2\pi)\int_0^{2\pi} \exp[in\beta]\exp[-i\gamma\sin(\beta)]d\beta$, Eq. (10) can be simplified as

$$P(L,\theta,z) = A_0 \exp\left[i\frac{2\pi}{\lambda}\sin(\alpha)z\right]\exp\left[-ir_0\frac{2\pi}{\lambda}\right] \times 2\pi\exp\left[i\left(\theta - \frac{\pi}{2}\right)\right]J_1(k_rL). \quad (11)$$

The term without azimuthal dependence in Eq. (11) is $A_1 = 2\pi A_0$. By substituting A_1 into Eq. (11), the pressure field is written as

$$P(L,\theta,z) = A_1 \exp\left[i\frac{2\pi}{\lambda}\sin(\alpha)z\right] \times \exp\left[i\left(\theta - \frac{\pi}{2} - 2\pi\frac{r_0}{\lambda}\right)\right]J_1(k_rL). \quad (12)$$

From Eq. (12), we can obtain that although k_r changes during propagation along the z axis, the effect on the generated Bessel beam is negligible, and the phase change along the z axis is mainly determined by $2\pi z\sin(\alpha)/\lambda = k_z z$. Taking the emission point located at the initial radius r_0 as an example, $\sin(\alpha)$ can be expressed as $z/\sqrt{r_0^2+z^2}$. After the integration, the phase change along the axis of the transmitted acoustic wave in the propagation process can be expressed as $\varphi_z = 2\pi\left[\sqrt{r_0^2+z^2} - r_0\right]/\lambda$, as shown in Fig. 4(e). It can be clearly seen that the speed of the phase change can be manipulated by changing the initial radius r_0. Here, we take the single-arm Archimedes-spiral slit as an example for analysis, and the sound field expressions of other arms can also be obtained by similar methods.

In other words, by changing the number of arms of the Archimedes spiral, we can realize Bessel vortex beams of different orders within a certain propagation distance. By changing r_0, k_z can be adjusted. Based on these two

conditions, we plan to implement RS-ABBs by superimposing Archimedes spirals with different initial radii r_0 and different numbers of arms n.

V. IMPLEMENTATION WITH ARTIFICIAL STRUCTURE PLATE

Figure 5 shows the case of RS-ABBs with asymmetry parameters c of 0.7 and 2.2 realized by using artificial structure plates engraved with Archimedean-spiral slits. The initial order l of both is fixed at 1. First, referring to step 3 in Fig. 3, it is obtained that when the asymmetry parameters are 0.7 and 2.2, the compositions of the increased orders m are (0, 1) and (1, 2, 3), respectively. Therefore, the final compositions of the Bessel modes n are (1, 2) and (2, 3, 4). Figure 5(a) shows a schematic diagram of the artificial structure formed by the superposition of spirals with different numbers of arms. The

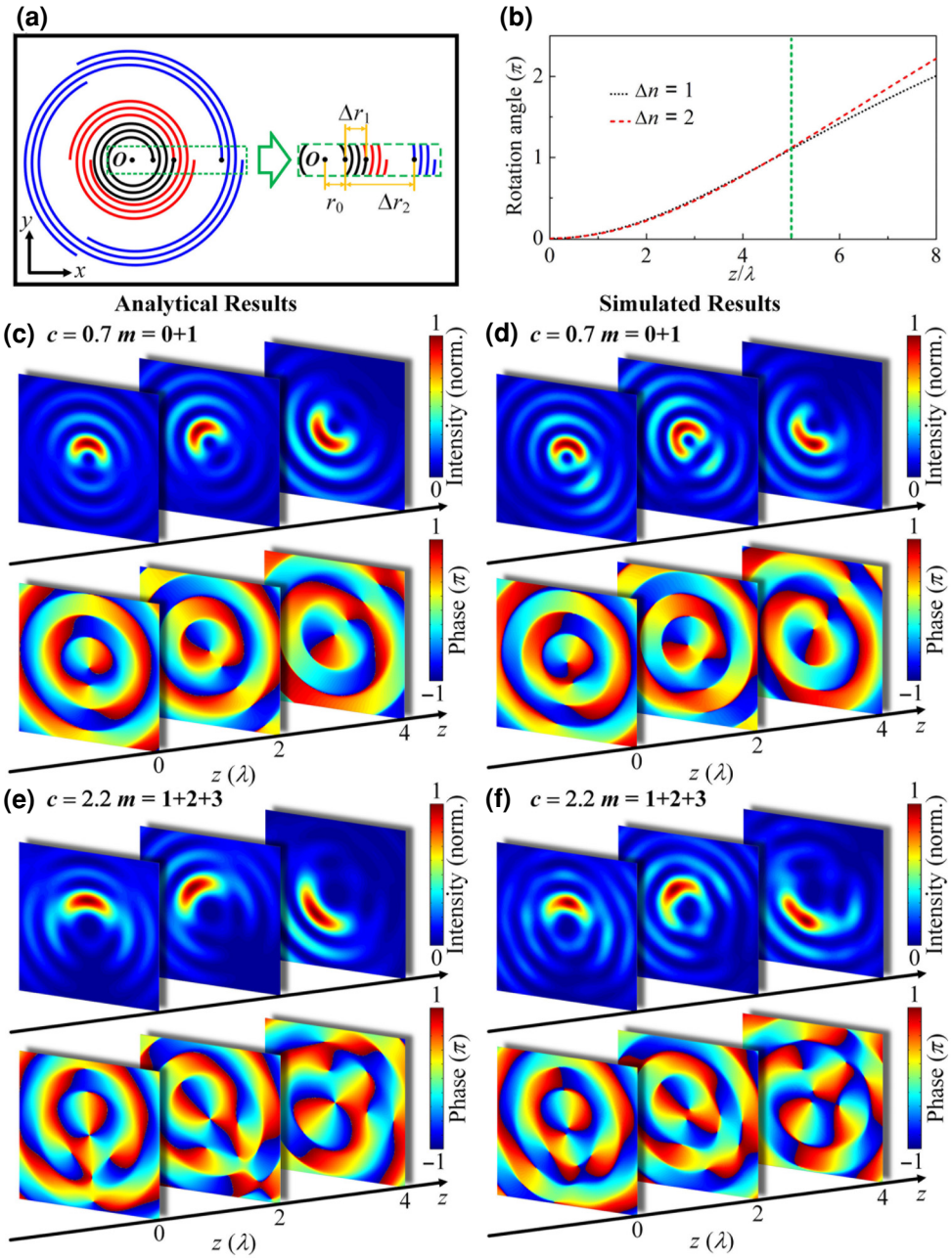

FIG. 5. (a) Schematic diagram of the artificial structure formed by the superposition of spirals with different numbers of arms. (b) Variation in the angular velocity of different Δn values with the propagation distance. (c) Analytical and (d) simulated acoustic intensity and phase distributions with $c = 0.7$ at three transverse planes of $z = 0$, $z = 2\lambda$, and $z = 4\lambda$. (e) Analytical and (f) simulated acoustic intensity and phase distributions with $c = 2.2$.

order of the superimposed Bessel modes can be determined by the number of arms of the Archimedes spiral. Here, $n = 1$, 2, 3 is used as an example, and the case of n can be changed according to the desired c. For the RS-ABB to have the designed angular velocity, each superposed Bessel mode should have a specific k_z, which is negatively linearly related to the difference between the Bessel orders (Δn). As seen from Fig. 4(d), we can reduce k_z by increasing r_0 of the Archimedes spiral, so each superimposed Archimedes spiral should have a specific r_0. In the actual implementation, we can design the corresponding structure size through the parameters of the background media. Here, we take air as the background medium for verification. The mass density and sound speed of air are 1.21 kg m^{-3} and 343 m s^{-1}, respectively. The working frequency of the sound wave is fixed at 15 kHz. The structural parameters are $a = \lambda = 22.9$ mm and $d = 10$ mm. To make the generated RS-ABBs have longer diffraction distances and to make experimental observation easier, the number of turns of the Archimedes spiral with different numbers of arms is fixed at 3 [35]. Considering the effect of the change in r_0 on the phase and k_z, we set the structural parameters $r_0 = 12.8$ cm (5.60λ), $\Delta r_1 = 6.7$ cm (2.94λ), and $\Delta r_2 = 20.3$ cm (8.88λ). Based on the designed initial radii, the ω values of $\Delta n = 1$ and $\Delta n = 2$ are shown in Fig. 5(b). With increasing propagation distance, both ω values gradually increase, while the ω values of $\Delta n = 1$ and $\Delta n = 2$ are basically the same in the 5λ range. Therefore, the conditions for realizing RS-ABBs of different c are satisfied.

Figure 5(c) shows the acoustic intensity and phase distributions of the RS-ABB based on Eq. (4). The corresponding c is 0.7, the superimposed Bessel modes are $n = 1$ and 2, and ω is shown by $\Delta n = 1$ in Fig. 5(b). The rotational angle of the crescent-shaped acoustic intensity gradually increases as the propagation distance increases, which is consistent with the theoretical prediction. Then, we perform full-wave simulations based on the finite-element method (using COMSOL Multiphysics software) to further verify our design. Figure 5(d) shows the simulated acoustic intensity and phase distributions of the RS-ABB, which are in accord with the analytical results. Figures 5(e) and 5(f) show the analytical and simulated results, respectively, of the RS-ABB with asymmetry parameter $c = 2.2$. The simulation results match well with the analytical results. With increasing c, the asymmetry and off-axis distance increase of the RS-ABB increases, while ω is basically maintained compared with the case for $c = 0.7$. These results indicate that our artificial structures can generate RS-ABBs with different c values. During the rotation of the RS-ABB, the acoustic field can be viewed as two separate structures, with the dominant structure of the crescent-shaped intensity distribution located in the center region of the beam. The other structure is a ringlike structure with a lower average intensity and a larger distribution area. Power is exchanged periodically between the two structures [23,24]. Each of these structures gains and loses power in a manner directly related to their angular acceleration. Thus, the angular momentum of the entire acoustic field remains constant.

VI. EXPERIMENTAL DEMONSTRATION

To experimentally verify the generated RS-ABB, we measure the transmitted acoustic intensity distribution of an artificial structure. Figure 6(a) shows a schematic diagram of the RS-ABB generated by experimental verification. It is noted that when the RS-ABB is observed from a certain angle, its thickness is constantly changing during propagation, which is caused by the crescent-shaped beam shape rotating during propagation. The inset of Fig. 6(a) displays a photograph of an artificial structure plate sample engraved with Archimedean-spiral slits. The artificial structure plate sample is made of a polymethylmethacrylate plate by laser engraving technology. Except for the engraved spiral slits, this sample can be considered as an acoustic hard boundary in the air [36]. It can be seen that there are three kinds of arm numbers of Archimedes-spiral slits engraved on the artificial structure sample, which are $n = 2$, 3, and 4, respectively, and the number of turns of each kind of spiral is 3, which corresponds to the structure situation of Fig. 5(f). The geometric size of the structure sample is $120 \times 120 \times 0.8$ cm^3 and the active area is 8×8 cm^2. In the experiment, a loudspeaker (Enpar Type-PD2101) with a central frequency of 15 kHz ($\lambda = 22.9$ mm) is used to transmit a continuous-wave signal, and a microphone (1/4 in., B&K Type-4938-A-011) to receive the acoustic signal. The loudspeaker is placed at $z = 1.5$ m to generate an incident quasiplane wave. The movable microphone is mounted on a three-dimensional stepper motor, and the acoustic field behind the structure sample is scanned by this microphone with a 2.29-mm step size. A multianalyzer system (B&K Type-3160-A-042) is used to obtain the time-domain acoustic signal for a point in space over a period of time, and then the time-domain acoustic signal is Fourier-transformed to obtain the spectrum of the signal, from which the acoustic intensity field can be reconstructed.

Figure 6(b) shows the normalized measured acoustic intensity distributions of the RS-ABB with $c = 2.2$ at three transverse planes of $z = 5$ cm (2.18λ), $z = 10$ cm (4.37λ), and $z = 15$ cm (6.55λ). A similar crescent-shaped acoustic intensity field appears in three transverse planes, and the crescent-shaped intensity rotates with the transmission distance. Figure 6(c) shows the corresponding simulated acoustic intensity distributions. The unbinarized accurate results for RS-ABB with $c = 2.2$ are shown in Fig. 6(d) for comparison. The experimental results almost match the simulated results, and the generated RS-ABBs are also basically the same compared with the exact results. During

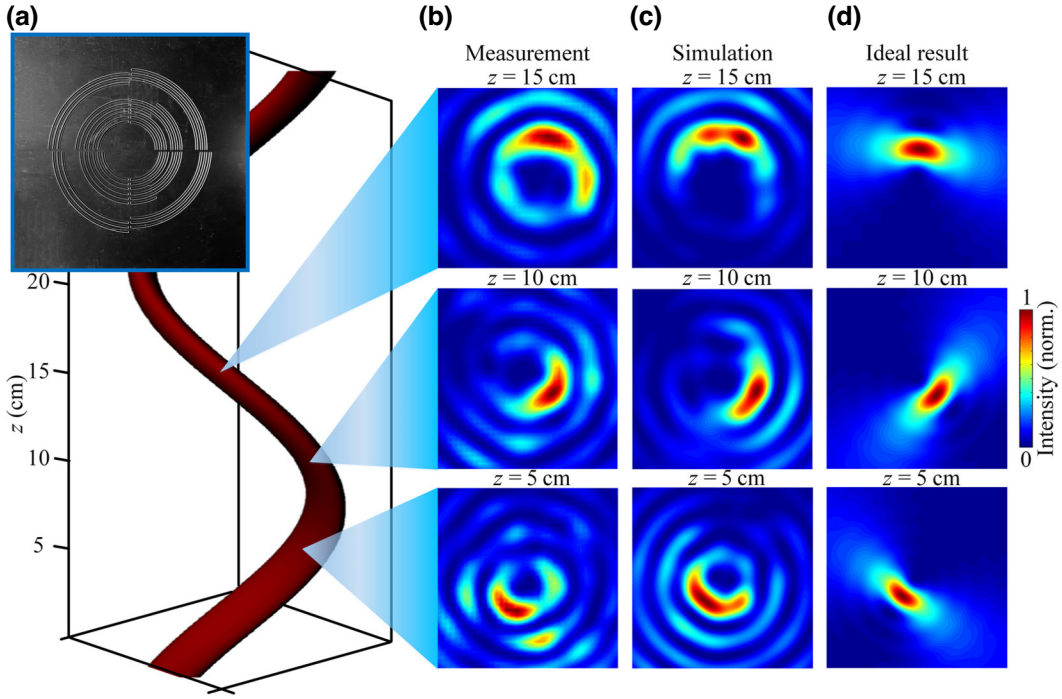

FIG. 6. (a) Photograph of an artificial structure plate sample for generating an airborne RS-ABB with $c = 2.2$. (b) Measured, (c) simulated, and (d) ideal acoustic intensity distributions of the RS-ABB at three transverse planes of $z = 5$ cm (2.18λ), $z = 10$ cm (4.37λ), and $z = 15$ cm (6.55λ).

the experiment, the incident acoustic waves generated by a single loudspeaker are difficult to perfectly represent in the simulation, which is the main reason for the deviation between the simulation and the experiment. In addition, the presence and imprecision of the three-dimensional stepper motor, sample fabrication, and inevitable viscous effect may all have an impact on the measured sound field. Based on the experimental results, we think that the proposed artificial structure could well generate the RS-ABB. Finally, we further investigate the frequency response characteristics of the generated RS-ABB (see Appendix B). The results show that when the operating frequency fluctuates between 5% (i.e., 14.25–15.75 kHz), there is still a good RS-ABB generation effect.

VII. CONCLUSION

In conclusion, we present a type of acoustic self-accelerating beam, referred to as an acoustic RS-ABB, characterized by a crescent-shaped acoustic intensity distribution that rotates with the distance traveled. The proposed RS-ABB exhibits remarkable asymmetry in the modulation capacity of acoustic intensity and orbital angular momentum, in tandem with potent wave-front manipulation capabilities. We derive the general analytical expression of RS-ABBs, which can be regarded as a superposition of an infinite number of Bessel modes with specific amplitudes and axial wave numbers. The shape of the crescent-shaped intensity can be independently modulated by the asymmetry parameters of asymmetric Bessel beams. In addition, we reveal that the axial wave number of the initial Bessel order has no effect on the rotating acoustic intensity field but is related to the phase distribution at different distances. A method is proposed that greatly simplifies the production requirements for RS-ABBs by binary conversion of the amplitudes of the superimposed Bessel modes. On this basis, an artificial structural plate with satisfactory performance for RS-ABB generation is further designed, which provides an effective prototype for implementation in practical applications. In addition, the RS-ABBs generated by the artificial structural plates are verified by numerical simulations and experimental measurements. Next, we can further calculate the acoustic radiation force situation when the RS-ABB acts on particles to provide theoretical support for the realization of directional particle transport. First, the incident beam is described as a sum of plane waves by the conventional angular spectral decomposition. The classical solution for the scattering of plane waves from an elastic sphere is then applied to each plane-wave component of the incident field. The incident and scattered waves can be superimposed in the far field to derive expressions for the radiative stress tensor components and to describe analytically the acoustic radiation force on the elastic sphere [37].

ACKNOWLEDGMENTS

This work was supported by the National Natural Science Foundation of China (12374439 and 12027808) and the Higher Education Institutions NSF of Jiangsu Province (23KJB140011).

APPENDIX A: INFLUENCES OF THE NUMBER OF APPROXIMATE BITS ON THE RESULTING RS-ABB

RS-ABBs consist of an infinite number of Bessel modes of different orders, each of which has a specific amplitude, which is determined by $c^m/m!$. We plan to use a simplified scheme, i.e., a multibit approximation of the amplitude of the superimposed Bessel modes. We binarize the amplitudes of Bessel modes of different orders by taking half of the maximum magnitude of the constituent Bessel modes at different values of c as a reference value, as shown in Fig. 7(a). The RS-ABB at $c = 3.7$ obtained by the two-bit approximation is shown in Fig. 7(b). In addition, we make a three-bit approximation to the amplitude of the superimposed Bessel modes, as shown in Fig. 7(c). We perform a three-bit approximation of the amplitude of the Bessel modes of different orders by taking 1/3 of the largest magnitude of the constituent Bessel modes at different values of c as reference value 1 and 2/3 of the largest magnitude as reference value 2. Bessel modes with amplitudes less than or equal to the reference value of 1 are ignored, and Bessel modes with amplitudes greater than the reference value of 1 are retained. We set the amplitude of Bessel modes with amplitudes greater than reference value 1 and less than or equal to reference value 2 to 1/2. We set the amplitude of Bessel modes with amplitudes greater than reference value 2 to 1. Figure 7(d) shows the RS-ABB at $c = 3.7$ obtained by the three-bit approximation. Similarly, we discuss the case of the four-bit approximation. Figures 7(e) and 7(f) show the results obtained using the four-bit approximation. We also show the untruncated accurate results in Figs. 7(g) and 7(h) for comparison. Comparing the results of different bit approximations, we find that when c is small (i.e., when there are fewer dominant Bessel modes), performing

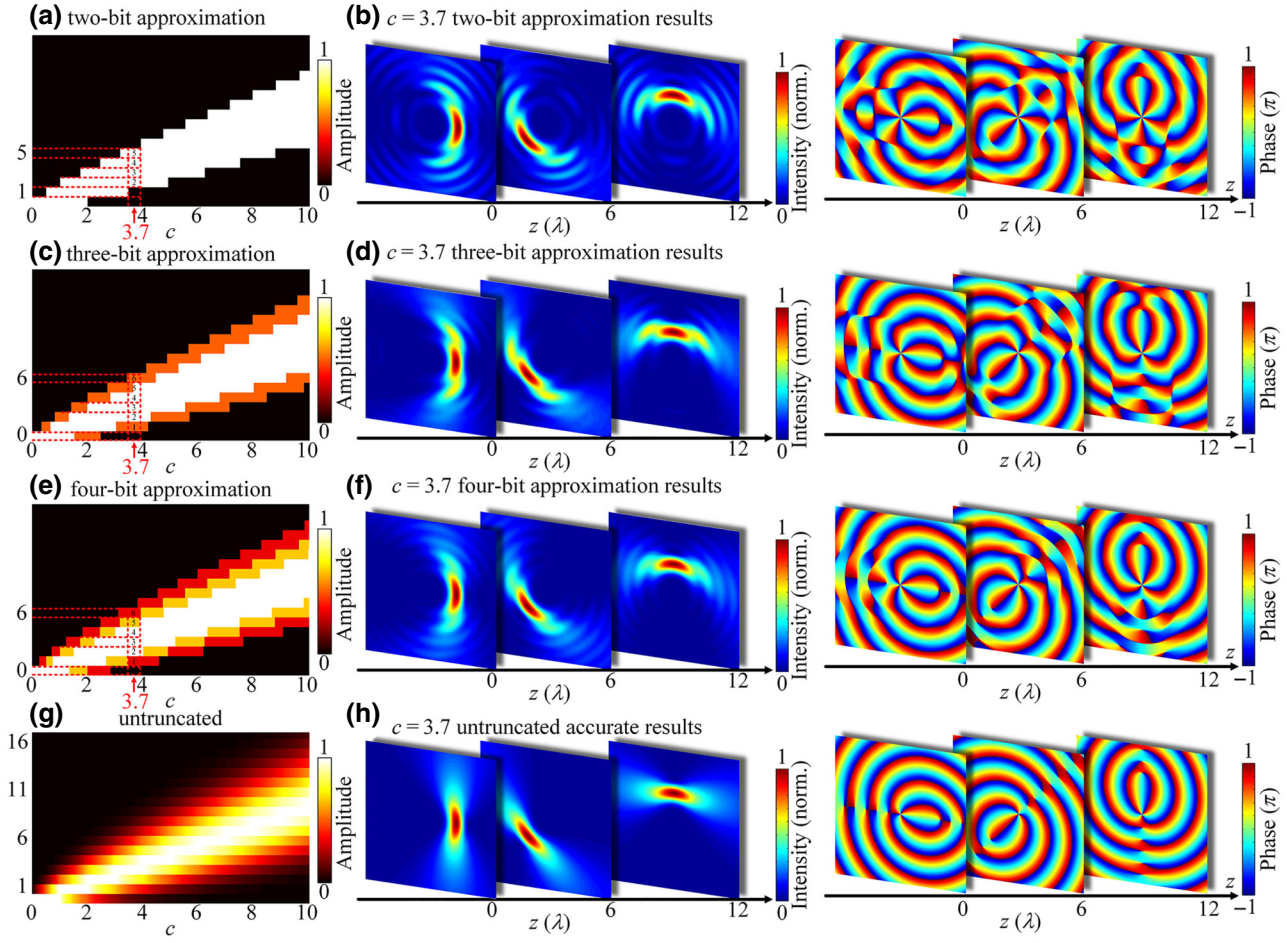

FIG. 7. The obtained RS-ABB with $c = 3.7$ using different bit approximations. (a),(b) The two-bit approximation, (c),(d) the three-bit approximation, and (e),(f) the four-bit approximation. (g),(h) The RS-ABB with $c = 3.7$ is obtained exactly without any approximation.

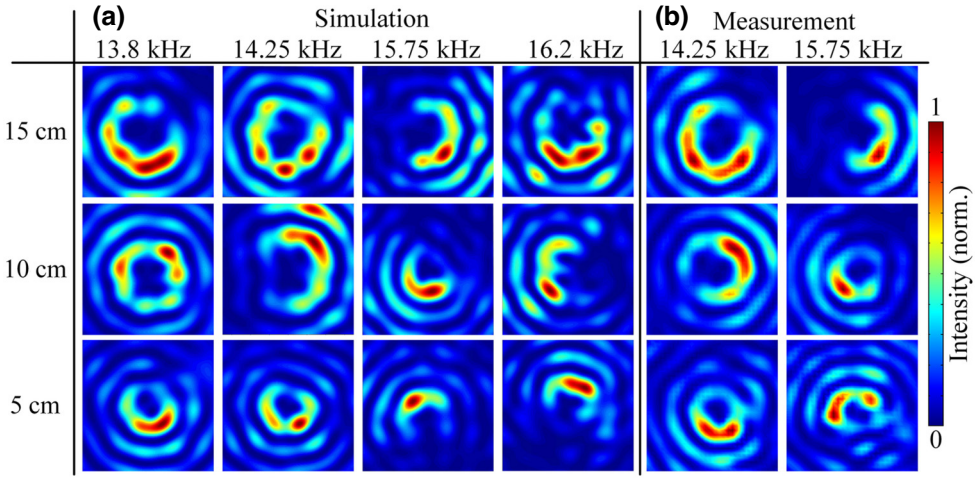

FIG. 8. (a) Simulated and (b) measured acoustic intensity distributions of the RS-ABB at different working frequencies.

a two-bit approximation is sufficient to well produce the RS-ABB, and that as the number of approximation bits increases, the RS-ABB obtained will converge more and more to the untruncated exact result.

APPENDIX B: INFLUENCES OF OPERATING FREQUENCY ON THE GENERATED RS-ABB

To further study the frequency response properties of the generated RS-ABB, we show the simulation results of the RS-ABB generated by the artificial structural plate at different frequencies, as shown in Fig. 8(a). The working frequency fluctuates 8%, i.e., the tested range is from 13.8 to 16.2 kHz. Due to the change in frequency, the initial position of the RS-ABB at $z = 0$ changes. Figure 8(b) shows the experimental results at 5% fluctuation of the operating frequency (14.25 and 15.75 kHz). The results show that when the operating frequency fluctuates between 5% (i.e., 14.25–15.75 kHz), there is still a good RS-ABB generation effect.

[1] X. Ren, Q. Zhou, Z. Xu, and X. Liu, Particle trapping in arbitrary trajectories using first-order Bessel-like acoustic beams, Phys. Rev. Appl. **15**, 054041 (2021).

[2] F. G. Mitri, Airy acoustical-sheet spinner tweezers, J. Appl. Phys. **120**, 104901 (2016).

[3] J. Huang, Q. Zhou, X. Ren, Z. Xu, and X. Liu, Acoustic manipulation on microbubbles along arbitrary trajectories and adjustable destination, Appl. Phys. Lett. **119**, 093503 (2021).

[4] P. Zhang, T. C. Li, J. Zhu, X. F. Zhu, S. Yang, Y. Wang, X. B. Yin, and X. Zhang, Generation of acoustic self-bending and bottle beams by phase engineering, Nat. Commun. **5**, 4316 (2014).

[5] S. Zhao, Y. Hu, J. Lu, X. Qiu, J. Cheng, and I. Burnett, Delivering sound energy along an arbitrary convex trajectory, Sci. Rep. **4**, 6628 (2014).

[6] H. Gao, Z. M. Gu, B. Liang, X. Y. Zou, J. Yang, J. Yang, and J. C. Cheng, Acoustic focusing by symmetrical self-bending beams with phase modulations, Appl. Phys. Lett. **108**, 073501 (2016).

[7] Y. Shen, Y. Peng, F. Cai, K. Huang, D. Zhao, C. Qiu, H. Zheng, and X. Zhu, Ultrasonic super-oscillation wavepackets with an acoustic meta-lens, Nat. Commun. **10**, 3411 (2019).

[8] Z. Li, K. Chen, F. Li, Z. Shi, Q. Sun, P. Li, Y. Peng, L. Huang, G. Yang, H. Zheng, and X. Zhu, Decorated bacteria-cellulose ultrasonic metasurface, Nat. Commun. **14**, 5319 (2023).

[9] D. Chen, X. Zhu, D. Wu, and X. Liu, Broadband Airy-like beams by coded acoustic metasurfaces, Appl. Phys. Lett. **114**, 053504 (2019).

[10] J. Baumgartl, M. Mazilu, and K. Dholakia, Optically mediated particle clearing using Airy wavepackets, Nat. Photonics **2**, 675 (2008).

[11] U. Bar-Ziv, A. Postan, and M. Segev, Observation of shape-preserving accelerating underwater acoustic beams, Phys. Rev. B **92**, 100301 (2015).

[12] Y. Zhang, Z. Mo, D. L. Xu, S. L. He, Y. P. Ding, Q. B. Huang, Z. L. Lu, and D. M. Deng, Circular Mathieu and Weber autofocusing beams, Opt. Lett. **47**, 3059 (2022).

[13] A. Libster-Hershko, I. Epstein, and A. Arie, Rapidly accelerating Mathieu and Weber surface plasmon beams, Phys. Rev. Lett. **113**, 123902 (2014).

[14] K. Tang, Y. Z. Hong, C. Y. Qiu, S. S. Peng, M. Z. Ke, and Z. Y. Liu, Making acoustic half-Bessel beams with metasurfaces, Jpn. J. Appl. Phys. **55**, 110302 (2016).

[15] X. Lu, X. Wang, S. Wang, and T. Ding, Polarization-directed growth of spiral nanostructures by laser direct writing with vector beams, Nat. Commun. **14**, 1422 (2023).

[16] F. Ju, W. Xiong, C. Liu, Y. Cheng, and X. Liu, Acoustic accelerating beam based on a curved metasurface, Appl. Phys. Lett. **114**, 113507 (2019).

[17] D. Chen, X. Zhu, Q. Wei, D. Wu, and X. Liu, Dynamic generation and modulation of acoustic bottle beams by metasurfaces, Sci. Rep. **8**, 12682 (2018).
[18] X. Li, H. Zhou, Y. Wang, and Y. Wang, Modulation of acoustic self-accelerating beams with tunable curved metasurfaces, Appl. Phys. Lett. **118**, 023503 (2021).
[19] Q. Zhou, X. Ren, J. Huang, Z. Xu, and X. Liu, Beam shaping in Fourier-transform acoustic systems, Phys. Rev. Appl. **20**, 024015 (2023).
[20] C. Vetter, T. Eichelkraut, M. Ornigotti, and A. Szameit, Generalized radially self-accelerating helicon beams, Phys. Rev. Lett. **113**, 183901 (2014).
[21] V. V. Kotlyar, S. S. Stafeev, A. G. Nalimov, S. Schulz, and L. O'Faolain, Two-petal laser beam near a binary spiral axicon with topological charge 2, Opt. Laser Technol. **119**, 105649 (2019).
[22] A. Mondal, Y. Xu, L. Andrew Wray, and D. G. Grier, Classically accelerating solenoidal wave packets in two dimensions, Phys. Rev. A **98**, 060101 (2018).
[23] J. Webster, C. Rosales-Guzmán, and A. Forbes, Radially dependent angular acceleration of twisted light, Opt. Lett. **42**, 675 (2017).
[24] C. Schulze, F. S. Roux, A. Dudley, R. Rop, M. Duparré, and A. Forbes, Accelerated rotation with orbital angular momentum modes, Phys. Rev. A **91**, 043821 (2015).
[25] P. Polynkin, M. Kolesik, J. V. Moloney, G. A. Siviloglou, and D. N. Christodoulides, Curved plasma channel generation using ultraintense Airy beams, Science **324**, 229 (2009).
[26] J. J. Jiang, D. L. Xu, Z. W. Mo, X. Z. Cai, H. Y. Huang, Y. Zhang, H. B. Yang, H. Q. Huang, Y. Wu, L. L. Shui, and D. M. Deng, Generation and control of tornado waves by means of ring swallowtail vortex beams, Opt. Express **30**, 11331 (2022).
[27] V. Anand, S. Khonina, R. Kumar, N. Dubey, A. N. K. Reddy, J. Rosen, and S. Juodkazis, Three-dimensional incoherent imaging using spiral rotating point spread functions created by double-helix beams, Nanoscale Res. Lett. **17**, 37 (2022).
[28] V. V. Kotlyar, A. A. Kovalev, and V. A. Soifer, Asymmetric Bessel modes, Opt. Lett. **39**, 2395 (2014).
[29] L. Gong, X. Qiu, Y. Ren, H. Zhu, W. Liu, J. Zhou, M. Zhong, X. Chu, and Y. Li, Observation of the asymmetric Bessel beams with arbitrary orientation using a digital micromirror device, Opt. Express **22**, 26763 (2014).
[30] V. V. Kotlyar, A. A. Kovalev, and V. A. Soifer, Superpositions of asymmetrical Bessel beams, J. Opt. Soc. Am. A **32**, 1046 (2015).
[31] X. Jiang, D. Ta, and W. Wang, Modulation of orbital-angular-momentum symmetry of nondiffractive acoustic vortex beams and realization using a metasurface, Phys. Rev. Appl. **14**, 034014 (2020).
[32] Y. Zhang, Z. Wu, G. Wu, P. Li, F. Wen, and Y. Gu, Controllable manipulation of composite multi-singularity vortex array, Opt. Commun. **495**, 127081 (2021).
[33] T. Wang, M. Ke, W. Li, Q. Yang, C. Qiu, and Z. Liu, Particle manipulation with acoustic vortex beam induced by a brass plate with spiral shape structure, Appl. Phys. Lett. **109**, 123506 (2016).
[34] H. Wang, L. Liu, C. Zhou, J. Xu, M. Zhang, S. Teng, and Y. Cai, Vortex beam generation with variable topological charge based on a spiral slit, Nanophotonics **8**, 317 (2019).
[35] N. Jiménez, R. Picó, V. Sánchez-Morcillo, V. Romero-García, L. M. García-Raffi, and K. Staliunas, Formation of high-order acoustic Bessel beams by spiral diffraction gratings, Phys. Rev. E **94**, 053004 (2016).
[36] L. Ye, C. Qiu, J. Lu, X. Wen, Y. Shen, M. Ke, F. Zhang, and Z. Liu, Observation of acoustic valley vortex states and valley-chirality locked beam splitting, Phys. Rev. B **95**, 174106 (2017).
[37] O. A. Sapozhnikov and M. R. Bailey, Radiation force of an arbitrary acoustic beam on an elastic sphere in a fluid, J. Acoust. Soc. Am. **133**, 661 (2013).